Biosensors and Bioelectronics 144 (2019) 111635

Contents lists available at ScienceDirect

Biosensors and Bioelectronics

journal homepage: www.elsevier.com/locate/bios

A novel sandwich aptasensor for detecting T-2 toxin based on rGO-TEPA-Au@Pt nanorods with a dual signal amplification strategy

Hangtian Zhong[a,b,1], Chao Yu[c,1], Rufei Gao[a,b], Jun Chen[c], Yujie Yu[a,b], Yanqing Geng[a,b], Yilin Wen[c], Junlin He[a,b,*]

[a] School of Public Health and Management, Chongqing Medical University, Chongqing , China
[b] Joint International Research Laboratory of Reproduction & Development, Chongqing Medical University, Chongqing, China
[c] College of Pharmacy, Chongqing Medical University, Chongqing, China

ARTICLE INFO

Keywords:
T-2 toxin
Aptamer
Dual signal amplification
Reduced graphene
Au@Pt nanorod

ABSTRACT

T-2 toxin is a mycotoxin that can cause chronic illnesses, and the detection of T-2 toxin in food is critical for human health. Herein, a novel sandwich aptasensor with a dual signal amplification strategy was developed for the detection of T-2 toxin. Molybdenum disulfide-polyaniline-chitosan-gold nanoparticles (MoS_2-PANI-Chi-Au) were processed to the modified glassy carbon electrode (GCE) and used as the aptasensor platform to expedite the electronics transport and immobilize the amino-terminated capture DNA probe by Au–N bonds. The reduced graphene oxide-tetraethylene pentamine-gold@platinum nanorods (rGO-TEPA-Au@Pt NRs) were first synthesized and immobilized with a signal DNA probe. Once T-2 toxin was added into the biosensing system, the aptamer would trap T-2 toxin to turn the signal off. Next, dissociative aptamer hybridized with the capture DNA probe in GCE and linked simultaneously to the signal DNA probe on rGO-TEPA-Au@Pt NRs with another end sequence of aptamer to turn the signal on. Owing to the efficient catalytic ability of bimetallic Au@Pt nanorods, the signal was perfectly amplified through the catalysis of hydrogen peroxide (H_2O_2) and recorded by chronoamperometry. With the outstanding augment response, the limit of detection reached 1.79 fg mL^{-1} ($3S_B/m$) and a wide linear range from 10 fg mL^{-1} to 100 ng mL^{-1} was presented. The sensitivity of the aptasensor was 19.88 $\mu A \cdot \mu M^{-1} \cdot cm^{-2}$. Meanwhile, the DNA aptamer-bimetallic nanorod based sensing system presented excellent specificity. The developed aptasensor provides a new platform for T-2 toxin detection with low cost for real sample assays.

1. Introduction

T-2 toxin, a type A trichothecene mycotoxin produced by Fusarium, is one of the most toxic food contaminants inevitably produced from cereal grains, especially in cold regions or under wet storage conditions (Gupta et al., 2011; Li et al., 2011; Pascale et al., 2012). Even low-dose T-2 toxin can penetrate the skin and inhibit the synthesis of DNA and RNA and have acute and subacute toxic effects on humans or animals after long-term exposure (Hossain and Maragos, 2018). Therefore, there is an urgent need for new monitoring systems to supervise the quality of foods. Traditional techniques such as high-performance liquid chromatography and high performance liquid chromatography-tandem mass spectrometry and gas chromatography (Gupta et al., 2011; Yue et al., 2009; Zou et al., 2012) are typically utilized for T-2 toxin determination. Although these assay methods show good accuracy and specificity, they have limited sensitivity and require expensive instruments (Chauhan et al., 2016). Recently, an electrochemical sensor has received significant attention as an alternative technique because of its high sensitivity, simple operation, low cost, and the potential for real sample analysis. Under these circumstances, pursuing the advantages of disposable biosensors and realizing the accurate detection of micromolecule T-2 toxin are worthy of consideration.

In the present study, the molybdenum disulfide-polyaniline-chitosan-Au nanoparticles (MoS_2-PANI-Chi-Au) were first assembled to modify the glassy carbon electrode and used as the sensor platform. In addition, MoS_2 with a large specific surface area and high electrical-conductivity (Guo et al., 2013; Shuai et al., 2017), PANI with high electrical conductivity was used to solve the inherent restacking or easy aggregation disadvantages of MoS_2 (Gan et al., 2017), synergetically increasing the conductivity by several orders of magnitude (Wu et al.,

* Corresponding author. Box 197#, No.1, Yi Xue Yuan Road, Yuzhong District, Chongqing Medical University, 1 Yi Xue Yuan Road, Chongqing, 400016, China.
E-mail address: hejunlin@cqmu.edu.cn (J. He).
[1] Chao Yu and Hangtian Zhong contributed equally to this work.

https://doi.org/10.1016/j.bios.2019.111635
Received 15 June 2019; Received in revised form 8 August 2019; Accepted 25 August 2019
Available online 28 August 2019
0956-5663/

2018). In this study, we also formed a chitosan film on the surface of MoS_2-PANI to enhance the stability and adhesion due to the presence of hydroxyl functional groups and reactive amino groups (Zhang et al., 2004). Finally, we reduced $HAuCl_4$ in situ on the surface to immobilize the capture DNA probe (CP), which is needed for the recognition of aptamer of T-2 toxin.

The recognition strategy is important to enhance the specificity of the sensor. Unfortunately, the traditional antigen-antibody detection strategy is far from satisfying the precision required for T-2 toxin detection. Since T-2 toxin is a micromolecule with non-immunogenic properties, the antibodies of T-2 toxin are not produced for the purpose of monitoring. Considering this limitation, the emergence of aptamer provides a shortcut. Similar to antigen-antibody interactions, aptamers combine with each of their target molecules through high specificity and affinity with some superior characteristics (Chen and Yang,2015). Research team (Chen et al., 2014) successfully screened out T-2 toxin aptamer and verified its practicability to propose a sensor for detection. Based on the aptamer sequence, we designed a target-triggering competition strategy. Since aptamer can recognize T-2 toxin in the microtube out of the electrode, the target-triggering competition strategy was activated once T-2 toxin appeared in the sensor system. After the competitive hybridization between aptamer and T-2 toxin, the toxin-aptamer mixtures were incapable for the sandwich structure construction due to the DNA sequence folding. Therefore, residual aptamer was added to the electrode for sandwich platform development. In the meantime, a total of two different single-stranded DNA sequences were synthesized. One of them with the complementary sequence match to the end sequence of aptamer was immobilized on MoS_2-PANI-Chi-Au by the Au–N bond on the electrode, and another DNA with the complementary sequence to the other end sequence of aptamer was linked to the signal material. Next, the aptamer sandwich platform was proposed successfully through the activation of the target-triggering competition strategy.

The signal amplification strategy plays an important role in the detection of low molecular weight molecules. Benefiting from the catalyst effect, various metallic alloys have been extensively studied (Thanh et al., 2017). We studied the unique electrochemical characteristics of Au and Pt and explored the Au@Pt nanorods (Au@Pt NRs). Under these circumstances, Au can afford long-term stability and biocompatibility while Pt can provide specific catalytic activity and combine with the amino-terminated signal DNA probe (SP) through Pt–N bonds. The structure of the nanorod makes it an adequate superficial area for catalysing hydrogen peroxide (H_2O_2). In order to further increase the catalytic performance for signal amplification, we need to find an ideal carrier to load more Au@Pt nanorods. Reduced graphene oxide-tetraethylene pentamine (rGO-TEPA) is well-known for its high conductivity, high surface area-to-volume ratio, and good biocompatibility (Ma et al., 2015). Its enhanced stability and hydrophilicity are profited from tetraethylene pentamine (Zhang et al., 2014). In addition, there are many amino groups discovered on the rGO-TEPA surface, making them a modifiable material for metal composition (Cao et al., 2017). Hence, rGO-TEPA was first modified with Au@Pt nanorods as the signal material and it achieved a higher catalytic efficiency.

In this study, we proposed a highly sensitive and innovative aptasensor for T-2 toxin detection based on MoS_2-PANI-Chi-Au as the substrate material and the rGO-TEPA-Au@Pt NRs as the signal material. However, the multitudinous target reaction system that occurs on the surface of the electrode may limit the recognition efficiency (Zhang et al., 2018; Zhao et al., 2014). Therefore, in this work, the recognition reaction between aptamer and T-2 toxin proceeded in microtubes with gentle shocking, avoiding the electrode surface area limitation. Owing to the superior augment response system, the aptasensor was successfully fabricated to detect T-2 toxin in food samples. The proposed aptasensor has a low detection limit, a wide linear range, and acceptable selectivity and reproducibility, which make it a promising method with applications in the food contamination field.

2. Experimental

2.1. Materials and chemicals

T-2 toxin was purchased from Fermentek Co., Ltd. The T-2 toxin plate kit was acquired from Hebei ELISA Biotech Co., Ltd. The canned beer was provided by Chongqing Beer Co., Ltd. The DNA oligonucleotides were obtained from Sangon Biotech Co., Ltd. (Shanghai, China). The DNA sequences are provided in Table S1. The detailed information on other chemical reagents, materials, and buffer solutions is exhibited in S1.

2.2. Apparatus and characterization

The detailed information on the apparatus and characterization is provided in S2.

2.3. Preparation of MoS_2-PANI

MoS_2-PANI was synthesized using the methods described in previous studies with appropriate adjustment (Bai et al., 2017). At the beginning of the experiment, 5 mg of MoS_2 and 5 mL ultrapure water were mixed and then sonicated for 10 min to obtain a homogeneous solution for further use. Next, 100 μL of aniline was added into 10 mL of the 0.5 M H_2SO_4 solution with continuous stirring (400 rpm), and then 10 mL of the 0.15 M $K_2S_2O_8$ solution was added dropwise into the above solution under rigorous stirring (700 rpm). Meanwhile, the prepared MoS_2 solution was added. The polymerization reaction proceeded at 0 °C for 4 h, and the colour of the mixture changed from transparent to dark green. After it was centrifuged ($6200 \times g$ 5 min^{-1}) and washed with ultrapure water for three times, the obtained MoS_2-PANI was dried in a vacuum freeze dryer and stored at 4 °C.

2.4. Preparation of MoS_2-PANI-Chi-Au

First, 2 mg of MoS_2-PANI was dissolved in 2 mL 1% acetic acid and sonicated until the solution became homogeneous. Next, 2 mg of chitosan was added into the mixture under constant stirring (1500 rpm). After that, 2 mL of 2% $HAuCl_4$ and 2 mL of 0.2 M $NaBH_4$ were slowly added into the solution under vigorous stirring (1500 rpm) for about 30 min. Finally, the obtained products were centrifuged at $16,200 \times g$ for approximately 5 min and washed for three times. The final precipitate was dispersed in 2 mL of ultrapure water for further use.

2.5. Synthesis of rGO-TEPA-Au@Pt nanorods

We proposed a practical method for the synthesis of Au@Pt NRs and prepared the Au NRs using the seed growth method (Tang et al., 2015).

2.5.1. Synthesis of Au seeds

First, 2.5 mL of 0.5 mM $HAuCl_4$ and 2.5 mL of 0.2 mM hexadecyl trimethyl ammonium bromide (CTAB) were mixed (500 rpm) in a beaker. Next, 300 μL of 0.01 M $NaBH_4$ was added by quick stirring (1000 rpm), and the reaction system was kept at 25 °C.

2.5.2. Growth of Au nanorod

First, we mixed 5 mL of 1 mM $HAuCl_4$ with 5 mL of 0.2 M CTAB under continuous stirring (500 rpm). Second, we slowly injected 0.15 mL of 4 mM $AgNO_3$ and waited for it to react for 5 min. Next, we added 70 μL of 0.079 M ascorbic acid and let it reduce for 2 min. At last, we injected 12 μL of the prepared Au seeds into the above solution by intensely stirring it (1000 rpm) for 20 s and left it for 2 h at 25 °C. After concentrating by centrifugation at $4700 \times g$ for 30 min, we extracted the supernatants and kept the residuum for further use.

2.5.3. rGO-TEPA-Au@Pt NRs synthesis

First, 0.1 mg of rGO-TEPA was mixed with 200 μL of the 20 mM CTAB solution by ultrasonication for 10 min to obtain the rGO-TEPA-CTAB complex solution, which is used for dispersing the Au NRs precipitate. Next, 20 μL of 10 mM H_2PtCl_6 and 10 μL of 0.1 mM ascorbic acid were injected into the solution. Finally, 20 μL of 10 mM Sodium hydroxide (NaOH) was injected to keep the reacted solution at alkaline conditions. The mixtures were centrifuged at 9600 × *g* for 5 min and washed for three times. The obtained compound was dissolved with 200 μL of ultrapure water for the next modification.

2.6. Synthesis of rGO-TEPA-Au@Pt NRs-SP

First, 200 μL of 4 μM amino-terminated SP was added into 1 mL of rGO-TEPA-Au@Pt NRs solution under stirring (100 rpm) at room temperature (25 °C) for 12 h. After centrifugation at 6200 × *g* for 5 min and washing for three times with ultrapure water, the precipitate was re-suspended in 1 mL of hybridization buffer and stored at 4 °C when not in use.

2.7. Sample treatment of canned beer

A concise, quick, and efficient process is required for real sample analysis. Hence, 50 mL of canned beer was poured into a 100 mL beaker and stirred at 200 rpm for 60 min at 60 °C. Next, it was sonicated for 30 min until completely degassed. After filtering through the 0.22 μm filter membrane, the pH of the beer sample was adjusted to 7 by adding the NaOH solution, and the pre-treated beer was stored at 4 °C.

2.8. Electrochemical aptasensor fabrication process

The construction process of the electrochemical DNA aptasensor is demonstrated in Scheme 1. In order to acquire a mirror-like surface, 0.3 μm or 0.05 μm alumina slurries were used for polishing the GCE, followed by ultrapure water rinsing. After ultrasonication with ultrapure water, absolute ethyl alcohol and ultrapure water in sequence, the electrode was exsiccated at room temperature (25 °C), and then 8 μL of MoS_2-PANI-Chi-Au nanocomposites was modified on the electrode. Next, 10 μL of CP (4 μM) was added to be incubated with MoS_2-PANI-Chi-Au nanocomposites at 4 °C for 12 h and immobilized through Au–NH_2 bonding. In order to remove nonspecific binding sites, 8 μL of 6-mercapto-1-hexanol (MCH) solution (1 mM) was coated for 30 min at room temperature (25 °C). In the meantime, 5 μL of T-2 toxin aptamer (2 μM) and 5 μL of multiple concentrations of T-2 toxin were mixed in the microtube and shocked gently at room temperature (25 °C) for 120 min to let T-2 toxin and T-2 toxin aptamer acquire a specific recognition process. Next, 10 μL of T-2 toxin and T-2 toxin aptamer mixed liquor were dropped onto the modified electrode and incubated at 37 °C for 120 min to let the redundant T-2 toxin aptamer hybridize with the CP immobilized on the modified electrode. Finally, 10 μL of the synthesized rGO-TEPA-Au@Pt NRs-SP bioconjugate was dropped onto the prepared electrode for hybridization with T-2 toxin aptamer at 37 °C for 2 h. The modified electrode was carefully washed with ultrapure water at each modification step. The electrochemical aptasensor was prepared for electrochemical analysis.

2.9. Electrochemical aptasensor detection process

At room temperature (25 °C), the electrochemical detection of amperometric i-t curves was performed in 5 mL of the working-buffer at the voltage of −0.4 V. Next, 20 μL of H_2O_2 (2.0 mol L^{-1}) was injected into the solution by gentle stirring until the background current became stable. After the electrochemical workstation collected signals for 100 s, the current changes were recorded.

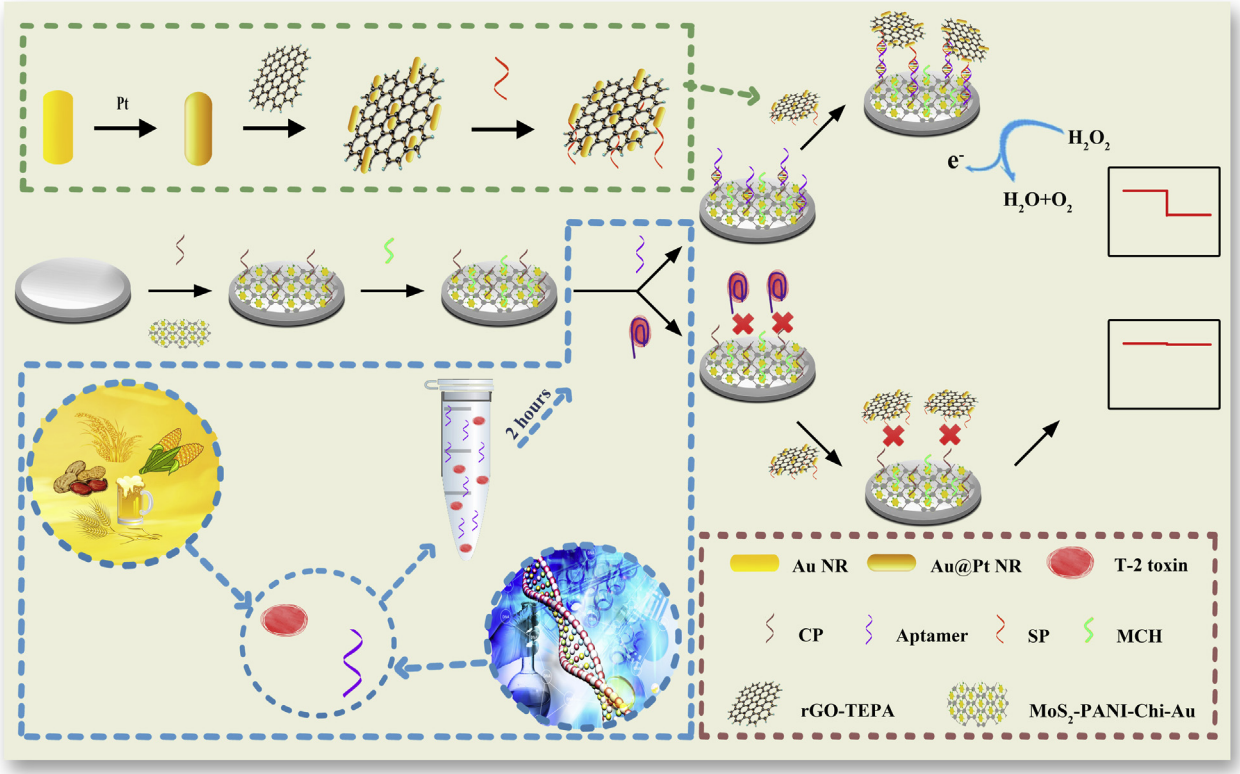

Scheme 1. Preparation process of rGO-TEPA-Au@Pt NRs-SP and schematic representation of the proposed strategy for the aptasensor.

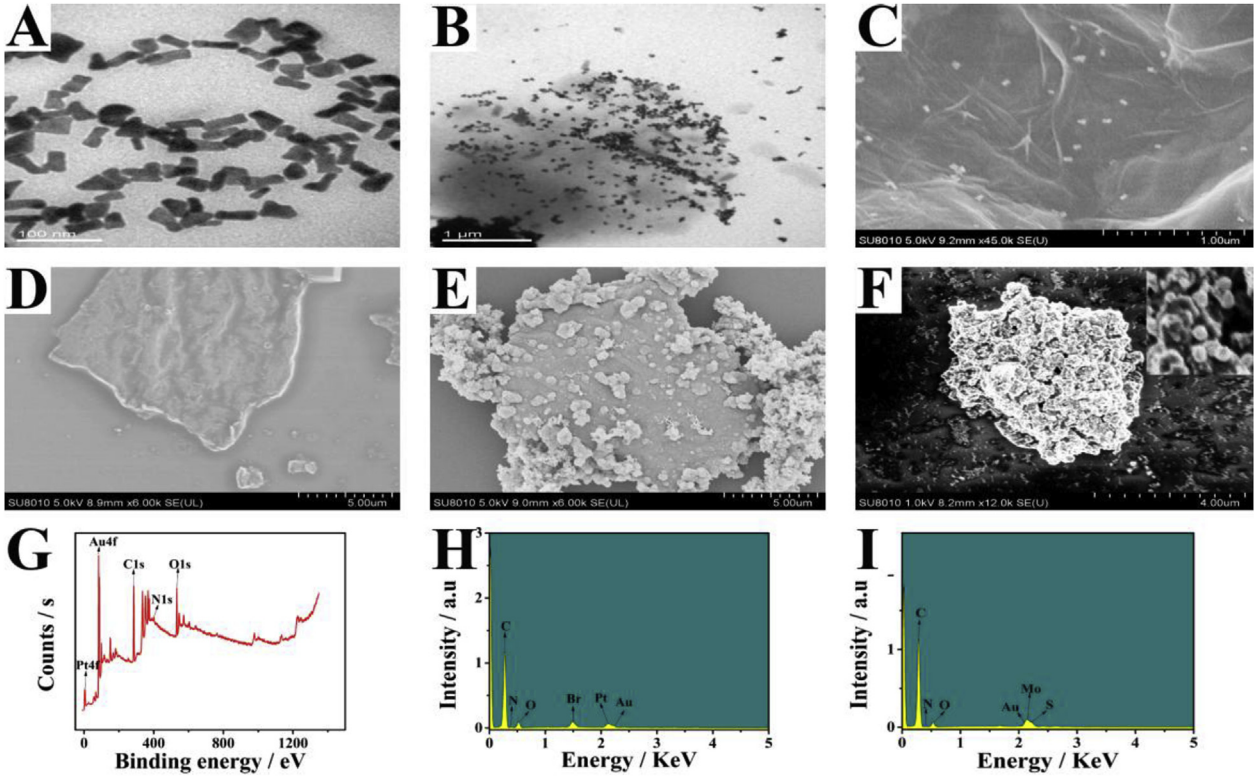

Fig. 1. TEM images of Au@Pt NRs (A), rGO-TEPA-Au@Pt NRs (B); FE-SEM images of rGO-TEPA-Au@Pt NRs (C), MoS_2 (D), MoS_2-PANI (E) and MoS_2-PANI-Chi-Au (F); XPS spectra of rGO-TEPA-Au@Pt NRs (G); EDS images of rGO-TEPA-Au@Pt NRs (H) and MoS_2-PANI-Chi-Au (I).

3. Results and discussion

3.1. Characterization of prepared nanomaterials

Transmission electron microscopy (TEM) and Field emission scanning electron microscopy (FE-SEM) were used to demonstrate the size and morphology of the prepared nanomaterials. As shown in Fig. 1A, the Au@Pt NR has a rough length of 80 nm and the distribution is relatively even. In order to load more Au@Pt NRs to amplify the signal, rGO-TEPA was used for the modified material. Fig. 1B and C show the TEM and FE-SEM images of rGO-TEPA-Au@Pt NRs respectively, in which Au@Pt NRs are interspersed evenly on the smooth and continuous surface of rGO-TEPA. The morphology of the MoS_2-PANI-Chi-Au nanocomposites was investigated using FE-SEM. As shown in the FE-SEM images of pure MoS_2, MoS_2-PANI, and MoS_2-PANI-Chi-Au (Fig. 1D–F), pure MoS_2 exhibited a regular laminar structure with some crumpled fold. After bonding with PANI obtained from the polymerization reaction, the surface of MoS_2 became relatively smooth because the compact original PANI layer was formed. The typical sponge-like porous surface morphology of PANI was also displayed at the edge of MoS_2. Finally, Au NPs were mass-modified on the surface of MoS_2-PANI-Chi by the in situ reduction of $HAuCl_4$. All these morphological verifications revealed that the nanomaterials were synthesized successfully.

To further confirm the effective synthesis of different nanomaterials, X-ray photoelectron spectroscopy (XPS) and Energy dispersive X-ray spectroscopy (EDS) were used for elemental analysis. The characteristic peaks for the Pt4f, N1s, C1s, Au4f, and O1s core level regions (Fig. 1G), which corresponded to the significant peaks of Pt, Au, C, O, and N in the EDS image (Fig. 1H), were successfully observed in the rGO-TEPA-Au@Pt NRs composites in the XPS image. Moreover, Figs. S1A–E illustrated the single XPS peak of C, N, O, Au, and Pt followed by their elemental mapping patterns. The element area profile shows that Au and Pt have a roughly accordant distribution, which indicates the successful synthesis of Au@Pt NRs. In the XPS image of the independent Au@Pt NRs in Fig. S2, the significant peaks of Pt and Au further support the results. The characteristic peaks of O, C, N, Au, Mo, and S appeared at MoS_2-PANI-Chi-Au nanocomposite (Fig. 1I). The core elements of the elemental mapping patterns of S, N, Mo, and Au are also shown in Figs. S3A–D. These results revealed the successful synthesis of different composites.

The FT-IR spectra, UV–vis absorption spectra, and ζ-potential were also used to demonstrate the required features of different nanocomposites. Corresponding data and figures are provided in S3.

To further indicate the stability of chitosan, we conducted static experiments of MoS_2-PANI-Chi and MoS_2-PANI. As shown in Fig. S7, after 20 h, MoS_2-PANI-Chi showed a more stable state than MoS_2-PANI.

Owing to the existence of Au NPs, electron transfer ability of MoS_2-PANI-Chi-Au nanocomposite significantly increased as demonstrated by the differential pulse voltammetry (DPV) measurement (Fig. S8).

3.2. Agarose gel electrophoresis analysis

Agarose gel electrophoresis was used to demonstrate the complementary base pairing of the single strand DNA designed in this study. As shown in Figs. S9 and 20 bp marker (lane A), CP (lane B), aptamer (lane C), and SP (lane E) exhibited the highest mobility because of their low molecular weights. As anticipated, the CP-aptamer (lane D) bioconjugates showed inferior mobility compared to CP and aptamer single strand because of the successful hybridization. SP and aptamer (lane G) conjugates exhibited the same effect as the CP-aptamer bioconjugates, which confirmed the successful hybridization of SP and aptamer. In addition, after the aptamer was hybridized with CP and SP, lane H exhibited the lowest mobility, confirming that aptamer was successfully hybridized with SP and CP. Finally, because CP and SP cannot be hybridized with each other, the band intensity of lane F was weakened. These results showed the hybridization feasibility of our aptasensor. The experimental results are shown in S4.

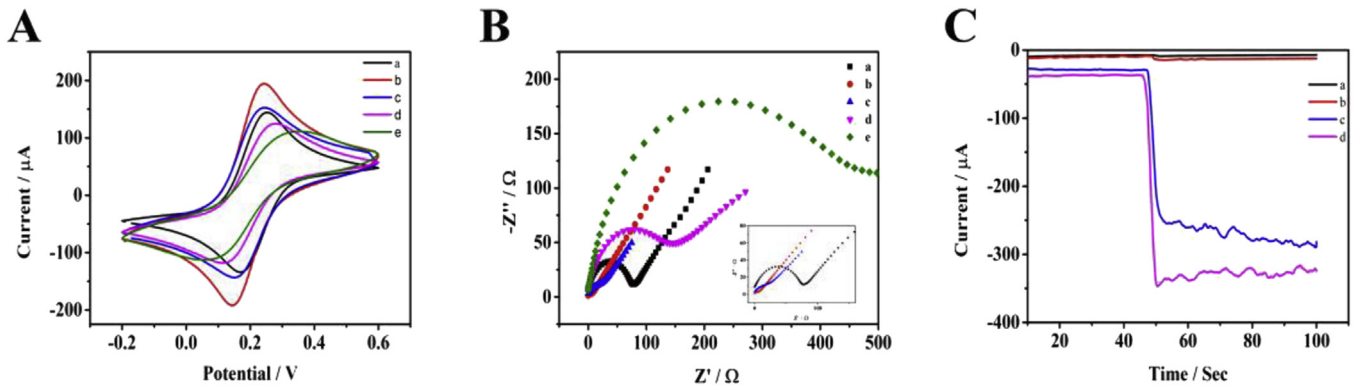

Fig. 2. (A) CV and (B) EIS characterization of electrodes at various stages of modification in a 5 mM $[Fe(CN)_6]^{3-/4-}$ solution: (a) bare GCE, (b) MoS_2-PANI-Chi-Au/GCE, (c) CP/MoS_2-PANI-Chi-Au/GCE, (d) MCH/CP/MoS_2-PANI-Chi-Au/GCE, (e) Aptamer/MCH/CP/MoS_2-PANI-Chi-Au/GCE; (C) Amperometric i-t curves of different nanomaterials modified electrodes after injection 20 μL of H_2O_2 (2.0 mol L^{-1}) into 5 mL of working buffer: (a) Au NRs/GCE, (b) rGO-TEPA-Au NRs/GCE, (c) Au@Pt NRs/GCE, (d) rGO-TEPA-Au@Pt NRs/GCE.

3.3. Electrochemical characterization of the stepwise aptasensor

Cyclic voltammetry (CV), differential pulse voltammetry (DPV) and electrochemical impedance spectroscopy (EIS) were used for the electrochemical characterization and detection of aptasensor electrodes during the stepwise construction process. The CV of modified electrodes at different stages was observed in the 5 mM $[Fe(CN)_6]^{3-/4-}$ solution. A typical redox peak was captured for the bare GCE (curve a in Fig. 2A). After being modified with MoS_2-PANI-Chi-Au, the electrode showed a significant increase in the peak current (curve b in Fig. 2A) because of the good electrical conductivity of MoS_2-PANI, while the electron transfer was remarkably strengthened by AuNPs. Curve c shows the redox peaks of CP-MoS_2-PANI-Chi-Au; because of the inferior conductivity of single strand DNA, the redox peak had a drastic decline. MCH had the same property as the single strand DNA; thus, the redox peak continued to decrease (curve d) after the MCH was immobilized on the electrode. Curve e exhibits the redox peaks when aptamer is hybridized with the CP immobilized on MoS_2-PANI-Chi-Au nanocomposites. This phenomenon can be ascribed to the abundant negative charges of DNA backbones and the electrostatic repulsion between the electroactive $[Fe(CN)_6]^{3-/4-}$; thus, the redox peak decreased to the lowest (Feng et al., 2018).

To further demonstrate the electrochemical characterization during the stepwise construction process, EIS was carried out. In the Nyquist diagram, the interfacial charge transfer resistance (R_{ct}) was reflected by the diameter of the high-frequency semicircle (Feng et al., 2018). Compared to the bare GCE (curve a), MoS_2-PANI-Chi-Au/GCE (curve b) showed a lower resistance in EIS (with an almost straight line) because of the accelerated electron transfer caused by MoS_2-PANI-Chi-Au nanocomposites (Fig. 2B). After incubating with CP (curve c), the resistance increased due to the single strand DNA can evidently hinder the electron transfer. As anticipated, the resistance progressively increased with the introduction of MCH (curve d). Finally, curve e shows the resistance when the aptamer hybridized with the CP immobilized on MoS_2-PANI-Chi-Au nanocomposites. Because of the inhibition effect of the negatively charged phosphate backbone, the resistance increased to the maximum level.

Differential pulse voltammetry (DPV) was used as a supplemental method. As shown in Fig. S10, the DPV curves increased after modifying with MoS_2-PANI-Chi-Au and then decreased after modifying with CP, MCH, and aptamer. With the alternating increasing and decreasing trends, the DPV curves also showed the successful construction of the aptasensor. Atomic force microscope (AFM) as an effective method to prove the interface properties of electrodes was used for electrochemical characterization during the stepwise construction process. A detailed description can be found in S5. The results confirmed the successful construction of the aptasensor.

3.4. Comparison of different signal nanomaterials strategies

The amperometric i-t curve of different signal amplification tags was compared to screen out the most valid signal amplification strategies. Au NRs showed negligible catalytic ability (curve a in Fig. 2). Because Au is a well-known metallic material with an extraordinary electrical conductivity but low catalytic ability. Even Au NRs were loaded with rGO-TEPA, the catalytic ability changed slightly (curve b). Curve c shows the i-t responses of Au@Pt NRs. After Pt was combined with Au NRs, the Au@Pt NRs nanocomposite exhibited an enhanced catalysis current compared to that without Pt. The function of rGO-TEPA was to support more Au@Pt NRs and strengthen the catalytic effect. The rGO-TEPA-Au@Pt NRs (curve d) displayed advantageous catalytic ability. These results demonstrate that the pairing of rGO-TEPA and Au@Pt NRs in this aptasensor has the greatest catalytic effect compared to the other materials during the experiment.

3.5. Optimization of the experiment conditions

The optimal electrochemical performance shows the sensitivity of the present electrochemical aptasensor. Therefore, some factors such as the volume of MoS_2-PANI-Chi-Au, the CP concentration, the CP and aptamer's hybridization time, and the concentration of H_2O_2 were carefully considered. We especially optimized the dosage of chitosan, which plays the role of the aptasensor.

The volume of MoS_2-PANI-Chi-Au not only indicates the sensitivity of the aptasensor but also has an effect on the quantity of CP immobilized on MoS_2-PANI-Chi-Au nanocomposites. Therefore, the volume of MoS_2-PANI-Chi-Au was in the range of 4–12 μL. As shown in Fig. 3A, the change in the current first showed an increase and then stabilized from 8 to 10 μL, suggesting that the amount of MoS_2-PANI-Chi-Au on the electrode surface was likely limited. Therefore, the optimal volume of MoS_2-PANI-Chi-Au was determined to be 8 μL.

The sensitivity of the aptasensor will be weak if the concentration of CP is low. If it is redundant, it will cause an unnecessary decrease in conductivity and be wasted. Fig. 3B exhibits the optimization routine from 2 to 6 μM of CP. As the concentration increases, the change in the current first increases and then becomes stabilized when the concentration of CP reaches 4 μM, which may be caused by the use of CP and the limited amount of Au seeds. Hence, 4 μM of CP was identified as the optimal concentration.

Whether the CP and aptamer were fully combined was affected by their hybridization time. Fig. 3C shows that the current increases from 60 to 120 min and a longer hybridization time has a negligible effect.

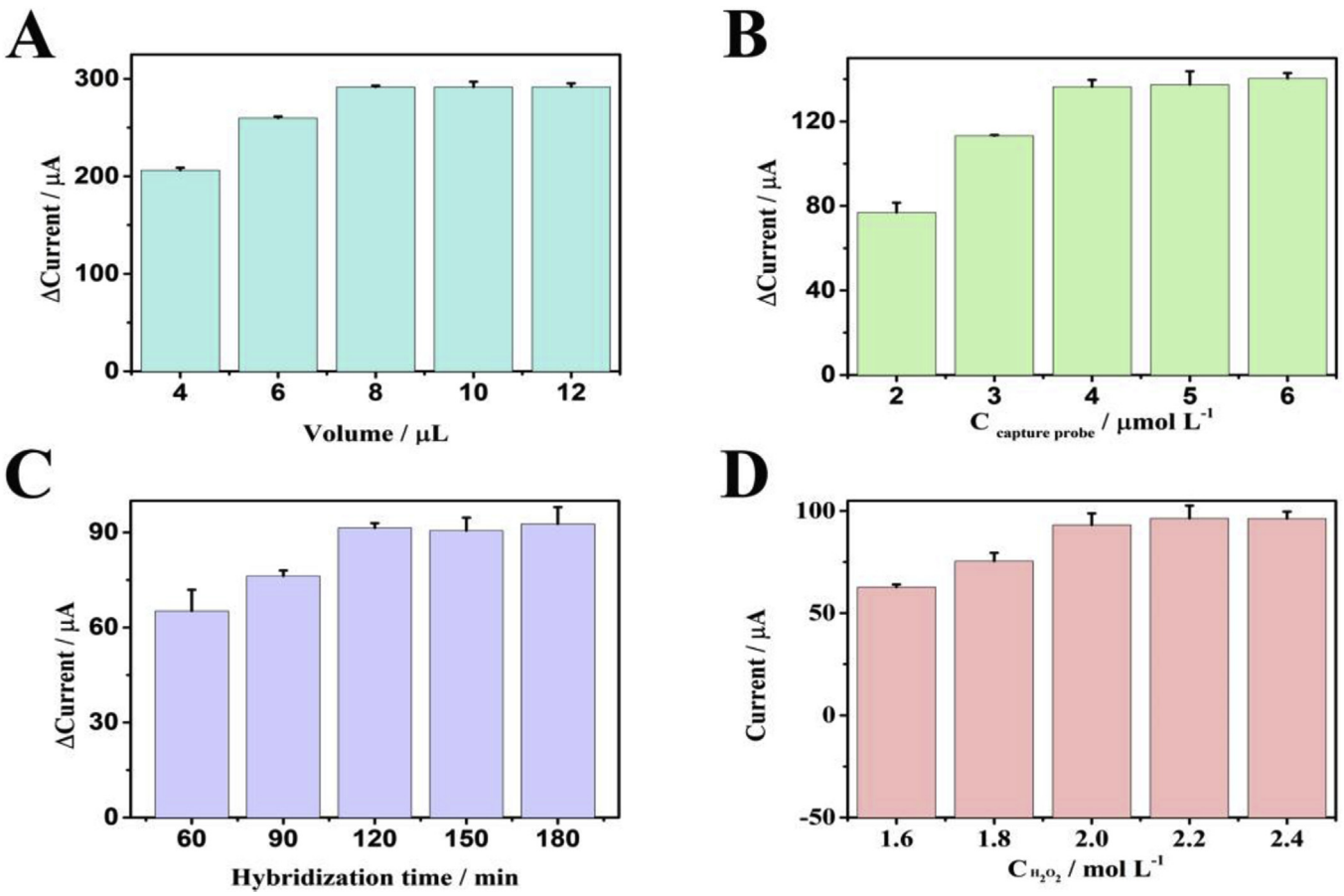

Fig. 3. Effects of (A) volume of the MoS_2-PANI-Chi-Au, (B) concentration of CP, (C) hybridization time, (D) concentration of H_2O_2.

Therefore, the optimal hybridization time was selected to be 120 min.

To achieve a higher catalysis efficiency, the concentrations of H_2O_2 were compared. As shown in Fig. 3D, the current was stabilized at 2 mol·L^{-1}, which indicates that the optimal concentration of H_2O_2 is 2 mol·L^{-1} in this study.

During the synthesis of MoS_2-PANI, we observed that the ability of MoS_2-PANI to transfer electrons was not steady. The experimental results suggested that the use of chitosan can effectively maintain the stability of MoS_2-PANI's conductivity. As a consequence, we optimized the usage amount of chitosan through CV scans for 50 cycles. According to the peak shape, we screened out the most standard and slender CV curves and ascertained the optimal usage amount of chitosan. As shown in Fig. S12, compared with the curve e, curve b is the most qualified peak shape and the corresponding usage amount of chitosan is 1 mg·mL^{-1}. The details of the optimized experimental conditions are given in S6.

3.6. Analytical performance of the aptasensor

The quantitative range and sensitivity of the proposed electrochemical aptasensor were evaluated by incubating the electrochemical aptasensor with different concentrations of T-2 toxin under optimal conditions. The changes in the amperometric i-t curve were captured after injecting 20 μL of H_2O_2 to the 5 mL of the working buffer for 100 s. As the T-2 toxin concentration increased from 0 to 100 ng·mL^{-1}, the i-t current response decreased gradually, which showed a negative correlation between the logarithm of the T-2 toxin concentration and the signal response (Fig. 4A). That's because when T-2 toxin is in the low concentration, there will be more free aptamers which can hybridize with the CP on the electrode and the SP combined with signal materials. Due to the increase of the signal materials, the catalytic signal is maximized and the reaction rate also in the high level. As the increasing of T-2 toxin, the aptamers in the reaction system decreased, which causing the fewer signal materials captured on the sensor. The decreased catalytic capacity results the weak electron transfer capacity in catalytic reactions, so the reaction rate gradually decreased. The standard curve is shown in Fig. 4B, which indicates a valid linear dependence of the current on the logarithm of the T-2 toxin concentration in the range of 10 fg·mL^{-1}–100 ng·mL^{-1}. The linear regression equation is $Y = -9.99*\log C_{T\text{-}2\ toxin} + 207.16$ ($R = 0.998$), and the limit of detection (defined as $LOD = 3S_B/m$, where m is the slope of the corresponding calibration curve and S_B is the standard deviation of the blank) (Bai et al., 2012)is 1.79 fg·mL^{-1}. According to the calibration plots between the i-t response and the logarithm of the T-2 toxin concentration and the geometrical surface area of working electrode, the sensitivity of the aptasensor was found to be 19.88 μA·μM^{-1}·cm^{-2} (Hooda et al., 2018; Lavin et al., 2018). These results indicate that the proposed electrochemical aptasensor has an excellent effect on the detection of T-2 toxin due to the unique signal amplification strategy and the superior detection strategy. We compared our work with other reported methods and the results are exhibited in Table 1. Owing to good conductivity and superior catalytic performance of the signal materials, we successfully produced and amplified the electrochemical signals. The comparison with other methods showed that the developed method achieved a superior performance with a lower detection limit.

3.7. Specificity, reproducibility and stability of the electrochemical aptasensor

During the detection of some real samples, some other mycotoxins might be present, which have the same species as T-2 toxin. In order to determine whether the other mycotoxins have an effect on the detection

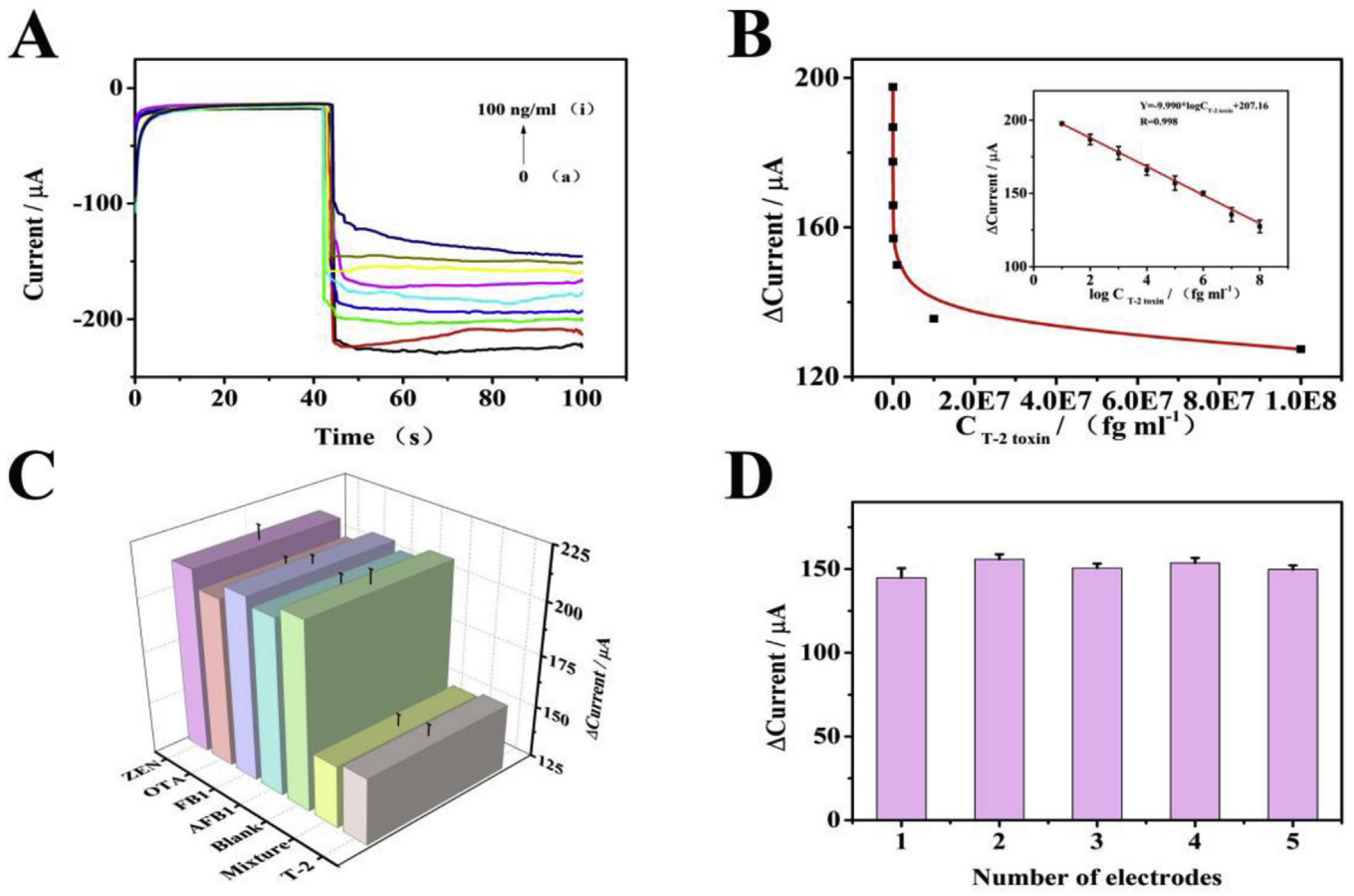

Fig. 4. (A) i-t curve signals of the aptasensor to determine different concentrations of T-2 toxin: (a) 0, (b) 10 fg·mL^{-1}, (c) 100 fg·mL^{-1}, (d) 1 pg·mL^{-1}, (e) 10 pg·mL^{-1}, (f) 100 pg·mL^{-1}, (g) 1 ng·mL^{-1}, (h) 10 ng·mL^{-1}, (i) 100 ng·mL^{-1}. (B) The calibration curve of the aptasensor for different concentrations of T-2 toxin (n = 3). (C) Selectivity of the aptasensor for the other four mycotoxins (ZEN, OTA, FB_1, AFB_1) (10 ng·mL^{-1}), zero analyte (Blank), a mixture (Mix) of the other four mycotoxins (10 ng·mL^{-1}) and T-2 toxin (100 pg·mL^{-1}). (D) Reproducibility of five different electrodes modified with 100 pg·mL^{-1} of T-2 toxin.

of T-2 toxin, we classified the mycotoxins into zearalenone (ZEA), ochratoxin (OTA), fumonisine B_1 (FB_1) and aflatoxin B_1 (AFB_1) to test their signal response. As seen in Fig. 4C, no significant current changes were captured compared to the blank assay. When other mycotoxins coexisted with T-2 toxin, the current response was nearly the same as when only T-2 toxin existed even if the concentrations of other mycotoxins were 100-fold higher than that of T-2 toxin. We also determined the specificity when T-2 toxin is at low concentration (Fig. S13). And the results are under acceptable limits. These results indicate that the electrochemical aptasensor exhibits high selectivity.

The reproducibility of the electrochemical aptasensor was demonstrated by using five different electrodes to detect 100 pg·mL^{-1} of the T-2 toxin under the same conditions. The relative standard deviation (RSD) of the present aptasensor was found to be 2.78% (Fig. 4D), which indicated the reproducibility of the electrochemical aptasensor. To further indicate the reliability of aptasensor, five different electrodes were used for the detection of 10 fg·mL^{-1} T-2 toxin and zero T-2 toxin under the same conditions. The RSD of the present aptasensor was found to be 1.78% (Fig. S14) and 1.68% (Fig. S15), respectively. Moreover, we discussed the repeatability of the sensor by using the same sensor for three times and recording the signals. The RSD of the present aptasensor was found to be 2.97%, which indicated reproducibility of the same electrochemical aptasensor. Finally, a long-term storage study was conducted to assess the stability of the electrochemical DNA aptasensor. During the storage process, the electrochemical aptasensors were stored at 4 °C for 3, 7, 14, and 21 d. After 21 d of storage, the aptasensor retained 85% of its initial current response because oligonucleotides had a gradual degradation process (Fig. S16). The results demonstrated the stability of the aptasensor under acceptable limits.

3.8. Analysis of T-2 toxin in simulated beer samples

The proposed aptasensor showed the merits of high sensitivity, simple operation, low cost, and potential for real sample analysis. Moreover, a concise, quick, and efficient process is required for real

Table 1
The results of comparing with other reported methods for the linear range and LOD of T-2 toxin.

Method	Linear range	LOD	Ref.
Molecularly imprinted	2.1 fM to 33.6 fM	0.1 fM (0.05 pg/mL)	Gupta et al. (2011)
Total internal reflection ellipsometry	0.15 ng/mL to 100 μg/mL	–	Nabok et al. (2007)
HPLC–MS/MS	0.05 μg/kg to100 μg/kg	0.007 μg/kg	Zou et al. (2012)
GC-ECD	50 μg/kg to 1000 μg/kg	2.5 μg/kg	Yue et al. (2009)
Electrochemical DNA sensor	10 fg·mL^{-1} to 100 ng·mL^{-1}	1.79 fg·mL^{-1}	This work

sample analysis. However, we did not obtain real samples for the T-2 toxin detection. In order to overcome this shortcoming, we used simulated beer samples in our experiments. For sample treatment, the beer sample was degassed by stirring, preventing the bubble from affecting the detection of T-2 toxin and aptamer. After filtering through the 0.22 μm filter membrane, the beer sample was purified by removing the foreign matter that could also have an adverse effect. Finally, the pH was adjusted to 7 to form the appropriate microenvironment for DNA. Sample preparations corresponded to the requirements of T-2 toxin detection in real samples.

To explain the electrochemical aptasensor's feasibility and precision in practical applications, a standard addition method (recovery experiment) was performed using the pre-treated canned beer samples. The gradient concentrations of T-2 toxin were added to the pre-treated canned beer samples to make the concentration 100 $fg \cdot mL^{-1}$, 100 $pg \cdot mL^{-1}$, and 10 $ng \cdot mL^{-1}$ for the electrochemical aptasensor measurement. As presented in Table S3, the recovery ranged from 94.62% to 103.52% and the RSD values ranged from 1.17% to 4.36%. The results are within the acceptable limits, which proved that the electrochemical aptasensor can be successfully applied to detect T-2 toxin in simulated beer samples. Moreover, the beer samples have negligible influence on the detection performance of the aptasensor system, and the investigated materials involved in the aptasensor also have negligible influence on the analyte.

To further illustrate the reliability of the electrochemical aptasensor, the developed method and the enzyme-linked immune sorbent assay (ELISA) method were used for analysing three simulated beer samples. As exhibited in Tables S4 and S5, the recovery of the developed method ranged from 95.10% to 101.90% and the RSD values ranged from 0.14% to 0.58%. The recovery of the ELISA method ranged from 75.19% to 113.48% and the RSD values ranged from 0.23% to 7.14%. Moreover, the two methods' relative errors were −10.81%–35.52% (Table S6). These results indicated the consistency between the two analytical methods. The results also showed that the developed method had a higher detection accuracy than the ELISA method.

4. Conclusion

We exploited a novel electrochemical aptasensor for the detection of T-2 toxin. Based on the first application of rGO-TEPA-Au@Pt NRs and MoS_2-PANI-Chi-Au, we improved the conductivity and sensitivity of the electrode. The proposed target-triggering competition strategy offers a new direction for the detection of T-2 toxin. The aptasensor showed a wide detection range, a low detection limit, good specificity, acceptable stability and reproducibility, indicating a novel method for the determination of T-2 toxin in the food safety field. This fabricated aptasensor offers a promising technique for the trace detection of low molecular weight compounds. A limitation of this study is that we did not obtain real samples for the T-2 toxin detection. In order to overcome this shortcoming, we used simulated beer samples in our experiments. Thus, in future work, we will collect real samples to further prove the feasibility of the aptasensor for the detection of T-2 toxin.

CRediT authorship contribution statement

Hangtian Zhong: Writing - original draft. **Chao Yu:** Writing - review & editing. **Rufei Gao:** Software. **Jun Chen:** Formal analysis. **Yujie Yu:** Data curation. **Yanqing Geng:** Investigation. **Yilin Wen:** Validation. **Junlin He:** Funding acquisition.

Declaration of competing interest

The authors declare that they have no known competing financial interests or personal relationships that could have appeared to influence the work reported in this paper.

Acknowledgement

We are grateful for the financial support from the Chongqing Technology Innovation and Application Demonstration (social and livelihood type general) Project (No. CSTC2018jscx-msyb0008), the National Natural Science Foundation of China (No. 31571554; No. 81370403), the Chongqing Foundation and Advanced Research Project (No. CSTC2015jcyjBX0053), and the Outstanding Graduate Student Cultivation Program of Chongqing Medical University (No. BJRC201807).

Appendix A. Supplementary data

Supplementary data to this article can be found online at https://doi.org/10.1016/j.bios.2019.111635.

References

Bai, L., Chen, Y., Bai, Y., Chen, Y., Zhou, J., Huang, A., 2017. Biomaterials 133, 11–19.
Bai, L., Yuan, R., Chai, Y., Zhuo, Y., Yuan, Y., Wang, Y., 2012. Biomaterials 33, 1090–1096.
Cao, L., Fang, C., Zeng, R., Zhao, X., Zhao, F., Jiang, Y., Chen, Z., 2017. Sens. Actuators B Chem. 252, 44–54.
Chauhan, R., Singh, J., Sachdev, T., Basu, T., Malhotra, B.D., 2016. Biosens. Bioelectron. 81, 532–545.
Chen, A., Yang, S., 2015. Biosens. Bioelectron. 71, 230–242.
Chen, X., Huang, Y., Duan, N., Wu, S., Xia, Y., Ma, X., Zhu, C., Jiang, Y., Wang, Z., 2014. J. Agric. Food Chem. 62, 10368–10374.
Feng, Q., Zhao, X., Guo, Y., Liu, M., Wang, P., 2018. Biosens. Bioelectron. 108, 97–102.
Gan, X., Zhao, H., Quan, X., 2017. Biosens. Bioelectron. 89, 56–71.
Guo, Y., Zheng, J., Ge, Q., Wang, S., 2013. Chin. J. Popul. Resour. Environ. 11, 283–287.
Gupta, G., Bhaskar, A.S., Tripathi, B.K., Pandey, P., Boopathi, M., Rao, P.V., Singh, B., Vijayaraghavan, R., 2011. Biosens. Bioelectron. 26, 2534–2540.
Hooda, V., Kumar, V., Gahlaut, A., Hooda, V., 2018. Prep. Biochem. Biotechnol. 48, 877–886.
Hossain, M.Z., Maragos, C.M., 2018. Biosens. Bioelectron. 101, 245–252.
Lavin, A., Vicente, J., Holgado, M., Laguna, M.F., Casquel, R., Santamaria, B., Maigler, M.V., Hernandez, A.L., Ramirez, Y., 2018. Sensors (Basel) 18.
Li, Y., Wang, Z., Beier, R.C., Shen, J., De Smet, D., De Saeger, S., Zhang, S., 2011. J. Agric. Food Chem. 59, 3441–3453.
Ma, H., Zhang, X., Li, X., Li, R., Du, B., Wei, Q., 2015. Talanta 143, 77–82.
Nabok, A.V., Tsargorodskaya, A., Holloway, A., Starodub, N.F., Gojster, O., 2007. Biosens. Bioelectron. 22, 885–890.
Pascale, M., Panzarini, G., Visconti, A., 2012. Talanta 89, 231–236.
Shuai, H.L., Huang, K.J., Chen, Y.X., Fang, L.X., Jia, M.P., 2017. Biosens. Bioelectron. 89, 989–997.
Tang, L., Li, S., Han, F., Liu, L., Xu, L., Ma, W., Kuang, H., Li, A., Wang, L., Xu, C., 2015. Biosens. Bioelectron. 71, 7–12.
Thanh, T.D., Balamurugan, J., Tuan, N.T., Jeong, H., Lee, S.H., Kim, N.H., Lee, J.H., 2017. Biosens. Bioelectron. 89, 750–757.
Wu, J., He, J., Zhang, C., Chen, J., Niu, Y., Yuan, Q., Yu, C., 2018. Biosens. Bioelectron. 102, 403–410.
Yue, Y.-T., Zhang, X.-F., Ou-Yang, Z., Gao, W.-W., Wu, J., Yang, M.-H., 2009. Chromatographia 70, 1495–1499.
Zhang, M., Smith, A., Gorski, W., 2004. Anal. Chem. 76, 5045–5050.
Zhang, W., Dixon, M.B., Saint, C., Teng, K.S., Furumai, H., 2018. ACS Sens. 3, 1233–1245.
Zhang, X., Li, F., Wei, Q., Du, B., Wu, D., Li, H., 2014. Sens. Actuators B Chem. 194, 64–70.
Zhao, Y., Liu, L., Kong, D., Kuang, H., Wang, L., Xu, C., 2014. ACS Appl. Mater. Interfaces 6, 21178–21183.
Zou, Z., He, Z., Li, H., Han, P., Tang, J., Xi, C., Li, Y., Zhang, L., Li, X., 2012. Meat Sci. 90, 613–617.